

# UV detectors aboard SOHO

W. T. Thompson

SM&A Corporation, Space Science and Engineering  
NASA Goddard Space Flight Center, Code 682, Greenbelt, MD 20771, USA

## ABSTRACT

A wide variety of ultraviolet detectors are used aboard the Solar and Heliospheric Observatory (SOHO) spacecraft. The ultraviolet instrument package aboard SOHO includes one full disk EUV flux monitor (SEM: 30.4 nm), one full sky mapper (SWAN: 121.6 nm), one full-Sun imager (EIT: 17.1–30.4 nm), and three spectrometers (CDS: 15.1–78.5 nm; SUMER: 66.0–161.0 nm; UVCS: 93.7–136.1 nm). All wavelengths are first order. In total, there are fifteen UV detectors aboard SOHO with six distinctly different designs. These range from photodiodes, through backside-thin CCDs, to two-dimensional microchannel-plate detectors. Some instruments measure an analog signal (such as the charge deposited in a CCD well), while others measure single photon events. The intense brightness of the Sun imposes unique challenges on these astronomical detectors. After almost three years of continuous observation in space, a large body of data has been gathered on their performance. How well each detector system has performed over this period is examined in turn.

**Keywords:** UV detectors, space missions

## 1. THE SOHO MISSION

The Solar and Heliospheric Observatory (SOHO) is a joint mission between the National Aeronautics and Space Administration (NASA) and the European Space Agency (ESA) to study the quiescent Sun. There are twelve instrument packages on board, which together study the solar interior with helioseismology, and the solar atmosphere with visible and ultraviolet imaging and spectroscopy. Six of these instruments observe the Sun in ultraviolet (UV) and extreme-ultraviolet (EUV) wavelengths, probing temperature structures ranging from 10,000 K to several million K. One instrument tracks the full disk EUV flux, an important parameter for planetary atmospheric modeling. Another instrument maps out the solar wind using scattered Lyman  $\alpha$ . A third provides full disk images at several selected wavelengths from 17–30 nm. The remaining instruments are spectrographs of various designs.

SOHO was launched on 2 December 1995. A “cruise phase” of several months was required for the spacecraft to reach its nominal orbit around the inner Lagrange point between the Earth and the Sun, although instrument operations generally began well before the end of this cruise phase. Operations then proceeded without interruption until 25 June 1998 when an accident caused SOHO to offpoint from the Sun and lose power for several months. Sun pointing was restored on 16 September 1998, and normal instrument operations were resumed a few weeks after that. During the interim when SOHO was pointed away from the Sun, the instruments experienced extreme temperature conditions, ranging from very hot ( $\geq 80^\circ\text{C}$ ) to very cold ( $\leq -50^\circ\text{C}$ ). We will consider the behavior of the instruments both during the first 2.5 years of continuous operations, as well as how the 3 months of temperature extremes affected them.

The ultraviolet detectors used on SOHO are of several different types, ranging from simple photodiodes to sophisticated photon-counting detectors. In between these extremes, one detector uses a backside-thin CCD, while another combines a CCD with a microchannel-plate intensifier. The intense brightness of the Sun imposes unique challenges on these astronomical detectors. After almost three years of continuous observation in space, a large body of data has been gathered on the performance of these detectors. Each detector system, and its performance over time, is examined below.

## 2. ANALOG DETECTORS

Three of the UV detector systems on SOHO work by detecting an analog signal. These detectors are in general well suited to the high flux rates seen from the Sun, while still providing good signal-to-noise characteristics. One system uses photodiodes, while the other two use cooled CCDs.

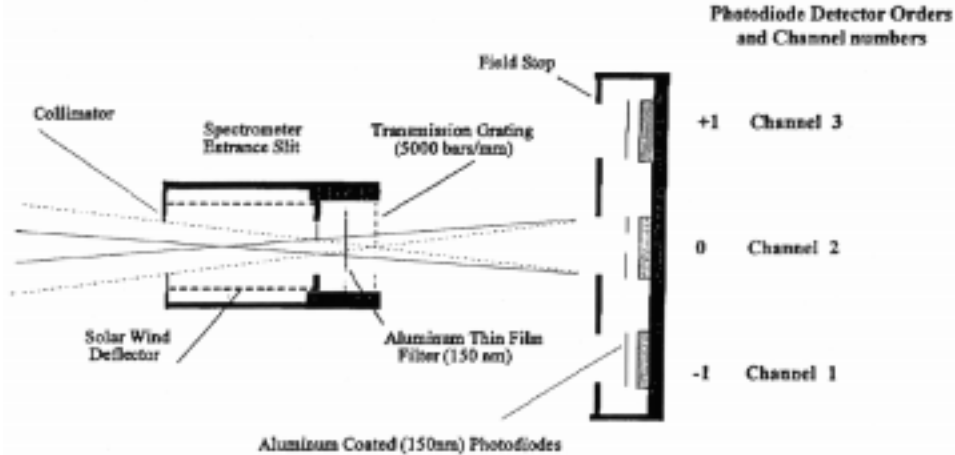


**Figure 1.** Schematic of the CELIAS Solar EUV Monitor (SEM).

### 2.1. SEM: A photo-diode based detector system

The Solar EUV Monitor<sup>1,2</sup> (SEM) measures the full disk absolute solar flux at the prominent He II 30.4 nm line, as well as the absolute integral flux between 17 and 70 nm. Unfocused light from the Sun passes through first a free standing aluminum filter (150 nm thick) to remove wavelengths above 70 nm, and then a free standing gold transmission grating (5000 lines/mm). The zero order and  $\pm$  first order 30.4 nm ( $\pm 4$  nm) radiation from the grating fall on three identical silicon photodiodes which are themselves coated with aluminum to further restrict visible light contamination (Figure 1).

The SEM detectors aboard SOHO appear to be highly stable. Comparison of the preflight calibration with an inflight cross calibration with a sounding rocket underflight of an “identical” SEM instrument on 26 June 1996 shows agreement to within 5%.<sup>3</sup> Comparison with another sounding rocket underflight on 11 August 1997 showed that the instrument degraded by less than 16% over the 14 month period. The two first order 30.4 nm channels track each other to a high degree of precision. All indications are that the detectors survived unscathed the extreme conditions during the months when SOHO was without power.

### 2.2. EIT: A backside-thin CCD

The Extreme-Ultraviolet Imaging Telescope<sup>4</sup> (EIT) takes full-disk images of the Sun in four wavebands centered on 17.1 nm (Fe IX), 19.5 nm (Fe XII), 28.4 nm (Fe XV), and 30.4 nm (He II/Si XI blend). The telescope (Figure 2) is a Ritchey-Chretien design with a 45 arcmin<sup>2</sup> field of view, and a spatial resolution limited only by the 2.6 arcsec pixel size of the CCD detector. The primary and secondary mirrors are separated into four quadrants; each quadrant has a different multilayer coating optimized for each of the four wavebands. A rotating mask at the front aperture selects between the wavebands. A heat rejection filter composed of 70 nm of cellulose sandwiched between 150 nm thick films of Al covers the EIT entrance aperture. Exposure is controlled via a mechanical shutter between the telescope and the detector.

The image from the selected waveband is focused on a thinned, back-illuminated CCD fabricated by SITe. The back surface has been processed to provide a high EUV quantum efficiency. The CCD is a  $1024 \times 1024$  array of  $21 \mu\text{m}$  square pixels with gate implants to provide Multi-Pinned Phase (MPP) operation. This provides lower thermal dark current, and better radiation hardness. Additional dark current and radiation damage control is obtained by cooling the CCD to about  $-67^\circ\text{C}$  by a cold finger attached to a passive radiator facing deep space. There are four readout ports, at the corners of the image array, with only one used at any time. The pixel full-well capacity is about 150,000 electrons, and the charge transfer efficiency is about 0.99995. A small heater is used to regulate the CCD temperature. A higher wattage heater allows the CCD to be warmed up to evaporate any condensates, and to anneal out any damage.

It was discovered that exposure to EUV radiation in flight did cause damage to the CCD detector.<sup>5</sup> When the median quiet-Sun intensity is plotted as a function of time, a steady loss of sensitivity can be seen (Figure 3a). This

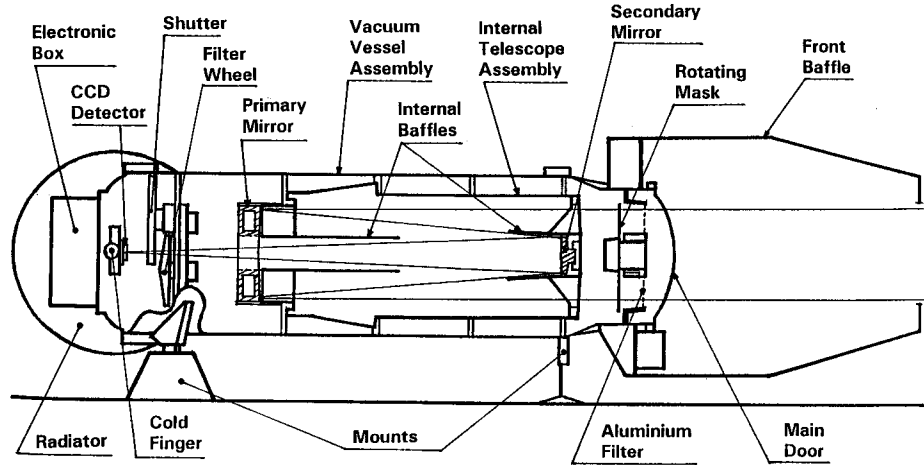


**Figure 2.** Schematic of the Extreme-ultraviolet Imaging Telescope (EIT).

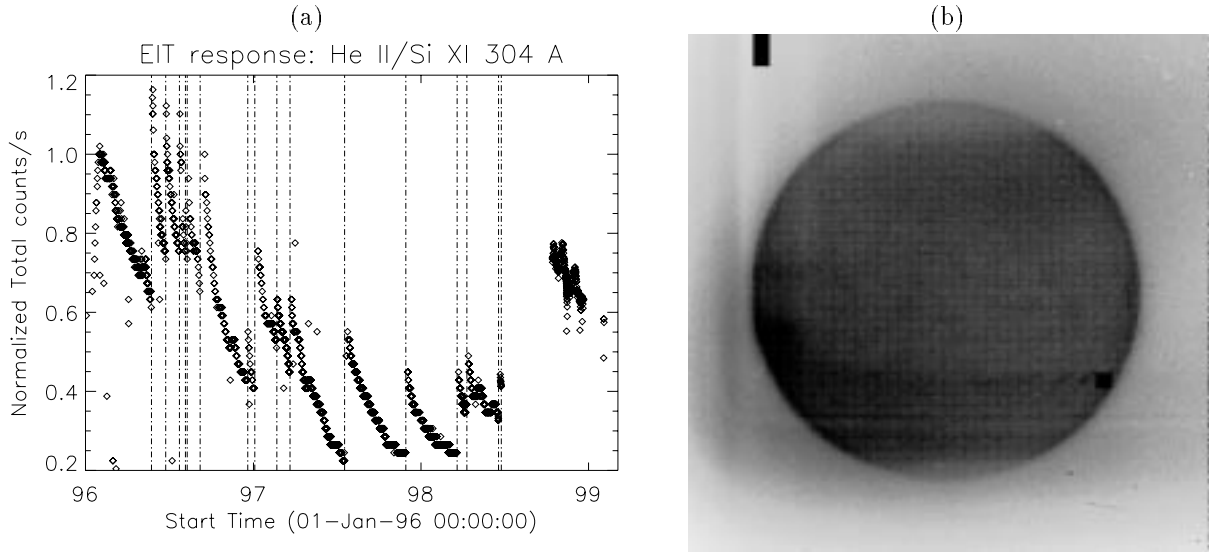


**Figure 3.** a) The relative median quiet-Sun solar intensity in the blended He II/Si XI 30.4 nm channel as a function of time. Dates when the CCD was heated (“bakeouts”) are marked as vertical dashed lines. There is an increase in sensitivity for each bakeout. An increase in sensitivity is also seen after the SOHO recovery in September 1998. b) Ratio of EIT flat field images taken using a visible light calibration lamp before and after bakeout, showing the preferential burn-in of the average solar image. The effect of solar limb brightening is clearly visible, as is the mesh supporting the aluminum filter in front of the detector. The effect of the burn-in in the EUV is wavelength dependent.

loss of sensitivity is highly localized on the detector, forming a negative image of the average solar disk (Figure 3b). Part of this sensitivity loss is due to condensates which collect on the cold surface of the CCD, but much of it appears to be related to damage within the CCD itself. Analysis of the image statistics shows that this damage results in a loss of charge collection efficiency, probably caused by the charging of the native backside oxide and the generation of interface trap sites. Periodically heating the CCD to 16.5°C anneals out some of this damage, as well as driving off condensates (mainly water ice) from the surface. During the period from July to September of 1998, when SOHO pointing control was lost, EIT was on the warm side of the spacecraft. This also led to an annealing of damage in the CCD, as can be seen in Figure 3.

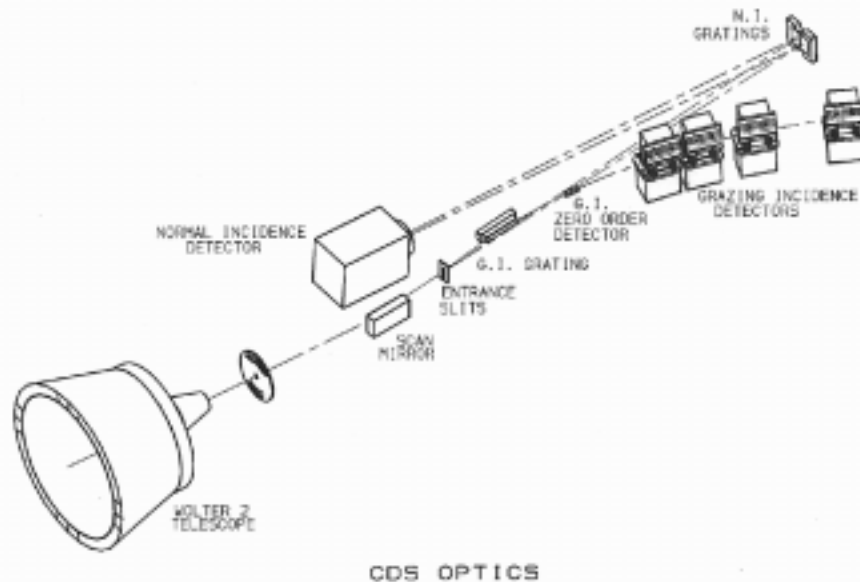


**Figure 4.** Optical layout of the CDS instrument.

### 2.3. CDS/NIS: An MCP intensified CCD camera

The Coronal Diagnostic Spectrometer<sup>6</sup> (CDS) consists of two spectrographs, one operating at normal incidence on the diffraction grating, and the other operating at grazing incidence. Both spectrographs are fed by a Wolter-Schwartzchild type 2 grazing incidence telescope, with different segments of the telescope used for each spectrograph (Figure 4).

In the Normal Incidence Spectrograph (NIS), the image from the telescope is focused onto a slit. Several slits of different widths can be selected, with angular widths of 2, 4, and 90 arcsec. All of the slits used with the NIS are 240 arcsec in height. A flat scan mirror placed between the telescope and the slit, operated at grazing incidence, allows two-dimensional images of the Sun to be built up through rastering. The light from the slit illuminates two normal-incidence toroidal gratings placed side to side, with different parts of the telescope illuminating each of the two gratings. The two dispersed spectra are stigmatically focused by the two gratings onto a two-dimensional detector placed on the Rowland circle. Both gratings are tilted slightly so that the two spectra do not overlap on the detector. One of the gratings focuses lines from 31–38 nm onto the detector, while the other operates from 51–63 nm.

The detector used for the NIS consists of a microchannel-plate intensifier placed in front of a CCD readout<sup>7</sup> (Figure 5). Unlike the other MCP detectors discussed below, this intensifier is operated at low voltage, and the signal measured consists of the accumulated charge deposited in the CCD wells during the exposure. Individual pulses are not counted. This allows the detector to operate at much higher count rates.

The microchannel plate is a single Philips device with 12  $\mu\text{m}$  pores on 15  $\mu\text{m}$  centers, and with an L/D of 40:1. The normal voltage across the MCP during an exposure is 756 V, although it can be varied anywhere from 600 V to 950 V. Between exposures, the MCP is held at a parking voltage of  $\sim 300$  V; shuttering is done by switching the voltage between the parking and operating values. No photocathode is deposited on the front of the detector; instead the detector relies on the photoelectric effect directly from the MCP. The electrons exiting from the back of the MCP are electrostatically focused onto a visible light phosphor deposited onto a fiber-optic output window. A lens focuses the visible light (green) output from the FO window onto the CCD.

The CCD used is a SITe device identical to that used for EIT, except that it is front-illuminated. The format is  $1024 \times 1024$  pixels, each 21  $\mu\text{m}$  on a side. Simultaneous readout from all four corners of the device is possible, although in flight it was decided to use only two corners to eliminate a feed-back loop within the electronics. A cold

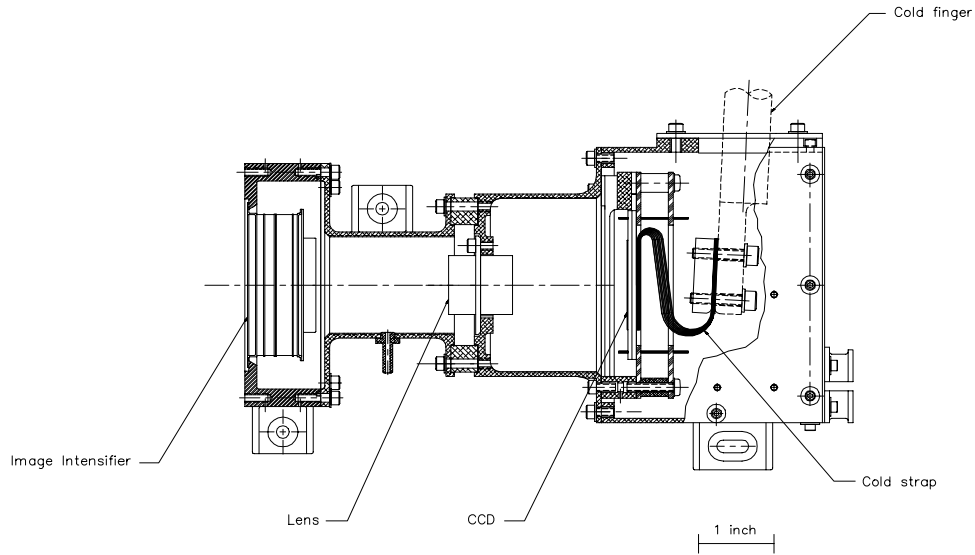


**Figure 5.** The CDS/NIS detector.

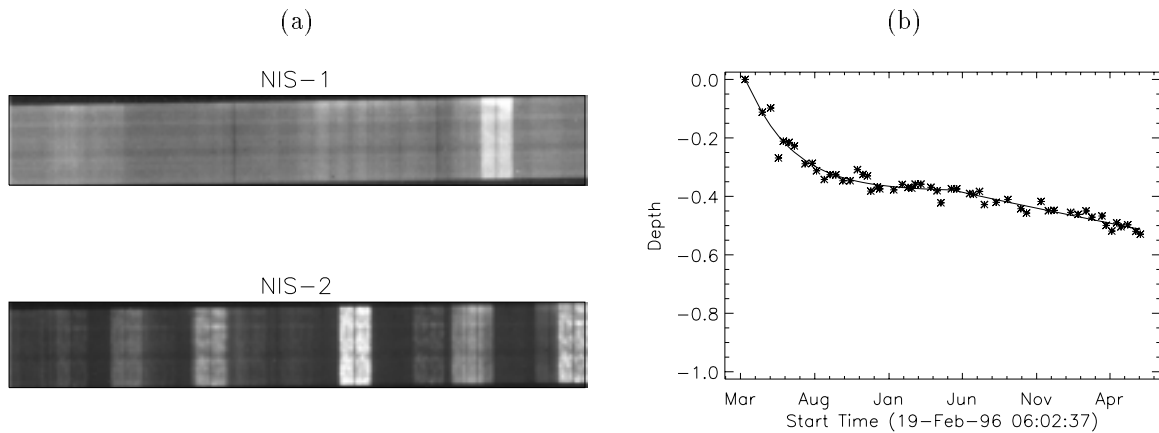


**Figure 6.** a) CDS/NIS images taken with the 90 arcsec wide slit, showing narrow slit burn-in. b) Measured depth of the narrow-slit burn-in at 58.4 nm as a function of time, relative to the total intensity. The value 0 represents no burn-in, and -1 represents complete burn-in. Since the He I line at 58.4 nm is the strongest line in the spectrum, it shows the greatest amount of burn-in. Also plotted is an analytic approximation for the data points.

finger attached to a passive radiator exposed to deep space cools the CCD to below  $-80^{\circ}\text{C}$ , for dark current and radiation damage control.

Since there is no wavelength selection mechanism on CDS, the solar emission lines always fall on the same pixels of the detectors. This leads to differential scrubbing of the MCP and exhaustion of the phosphor for those pixels. Most CDS/NIS observations are made with a narrow slit of either 2 or 4 arcsec width, and thus the greatest amount of “burn-in” occurs where the narrow-slit images fall. CDS also has a wider 90 arcsec slit. When this slit is used, the burn-in from the narrow slit is clearly visible as a dark band down the middle of each wide slit emission line image (Figure 6a). Images such as these are used to trace the history of the “burn-in” of each emission-line. The strongest line in the CDS/NIS spectrum is the He I emission line at 58.4 nm, and thus this line has the greatest amount of burn-in. Figure 6b shows the measured amount of narrow-slit burn-in over time at 58.4 nm. These measurements underestimate the total amount of burn-in on the detector, since they don’t include the burn-in due to the wider 90 arcsec slit. That slit is used less often than the two narrow slits. Thus, the burn-in effect from the wide slit is

smaller, but not negligible. Synoptic observations of the median quiet-Sun values are used to track the total amount of burn-in from both the narrow and wide slits, in a manner similar to the procedure used to track the efficiency of EIT (Figure 3).

As well as the depths of the burned-in lines, the exact positions and shapes of the burn-ins must also be measured, so the effect of the burn-in on the spectral line profile can be fully accounted for. The width of the heavily burned-in He I 58.4 nm line, after the burn-in corrections are applied, dropped by 8% between the start of the mission and loss of contact in June 1998, indicating that there is still a small error in modeling the wings of the burn-in profile. Other strong lines show similar, but smaller, amounts of narrowing.

Some improvement in sensitivity,  $\sim 19\%$ , was seen in the heavily burned in lines after recovery of the instrument in October 1998. This was most likely due to the high sustained temperatures that CDS was subjected to while attitude control was lost. When contact was first restored in August 1998, the CDS spectrometer box was measured at  $78.6^\circ\text{C}$ , and was the hottest instrument on the spacecraft. It is also now known that these high temperatures released contaminants that had previously been frozen onto the radiator and cold strap. These contaminants may be partially responsible for the reversal of the scrubbing of the MCP by the strong lines. Burned in areas on the phosphor, however, would not recover by this mechanism.

### 3. PHOTON COUNTING DETECTORS

Three of the UV detector systems on SOHO use microchannel-plate (MCP) amplifiers with anode readouts to count single photon events. This variety of detector design combines high sensitivity with signal-to-noise characteristics limited only by the Poisson statistics of the incoming photons. The main limitation of photon counting detectors for solar observations is their limited count rate capability. Also, the high gains required to be able to count a single pulse leads to accelerated degradation of the detector. These limitations restrict the targets that can be observed, but the detectors are still suitable under certain conditions.

#### 3.1. CDS/GIS: A spiral-anode detector

The CDS Grazing Incidence Spectrometer<sup>6</sup> (GIS) uses four detectors spread out over the Rowland circle, operating at 15–22 nm, 26–34 nm, 39–49 nm, and 66–79 nm. The GIS uses a spherical grating of 1500 mm radius of curvature, used at grazing incidence. The spectrum focused onto the detectors is astigmatic, so typical operation of the GIS uses pinhole apertures instead of the 240 arcsec slits used for the NIS. Rastering with the GIS is performed by moving both the scan mirror for horizontal motion, and the pinhole for vertical motion.

Because of the astigmatic nature of the GIS, the detectors are one-dimensional. The sensitive area of each detector is an open Z-stack of three MCPs. The MCPs are  $50 \times 25$  mm, with  $12.5 \mu\text{m}$  pores on  $15 \mu\text{m}$  spacing. Each EUV photon produces a cloud of  $\sim 4 \times 10^7$  electrons. Three adjacent anodes behind the MCP stack receive the electron cloud. These anodes have a special sinusoidal shape (Figure 7). When the signals from anodes  $X, Y, Z$  are plotted as  $X/(X + Y + Z)$  versus  $Y/(X + Y + Z)$ , then a spiral pattern is traced out (Figure 8a). For this reason, these are called Spiral Anode (SPAN) detectors. In normal operations, an on-board processor converts the signals from the three anodes into a position (wavelength) along the detector, using lookup tables. Each detector digitizes the spatial dimension into 2048 “pixels” of  $\sim 25 \mu\text{m}$  width.

As well as the normal science mode, the GIS detectors can also be operated in a “raw” mode, where individual photon events are telemetered down to the ground. These raw events allow the pulse height distribution to be determined, and the data are used to establish the lookup tables for normal science operations. Separate lookup tables are used for active region, quiet Sun, and coronal targets, as well as for each of the slit apertures used. Periodically, raw dumps of the detectors are taken for each of the separate operating conditions, to check that the lookup tables are still valid.

At some locations on the detector, the spiral will widen to the point that the spirals overlap. Spectral lines that fall on these detector locations will appear both at their nominal locations, and as “ghosts” at other regularly spaced locations on the detector. To completely characterize these lines, the counts in both the nominal and ghost locations must be summed together.

No degradation in the detector sensitivity has been detected during the mission, up until the loss of contact with the spacecraft in June 1998. After the recovery of the SOHO spacecraft in September 1998, the intensities in some lines were seen to drop by about 5% compared to pre-accident levels, while other lines were apparently unaffected.

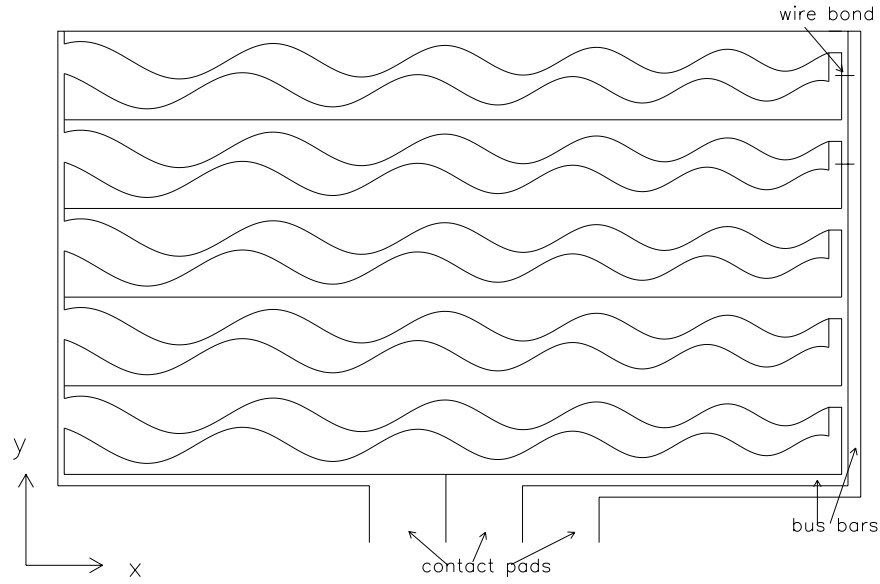


**Figure 7.** A schematic of the 1-D SPAN anode electrode configuration used for CDS/GIS. Position sensing is accomplished by measuring the charge in each of the three sinusoidal electrodes.

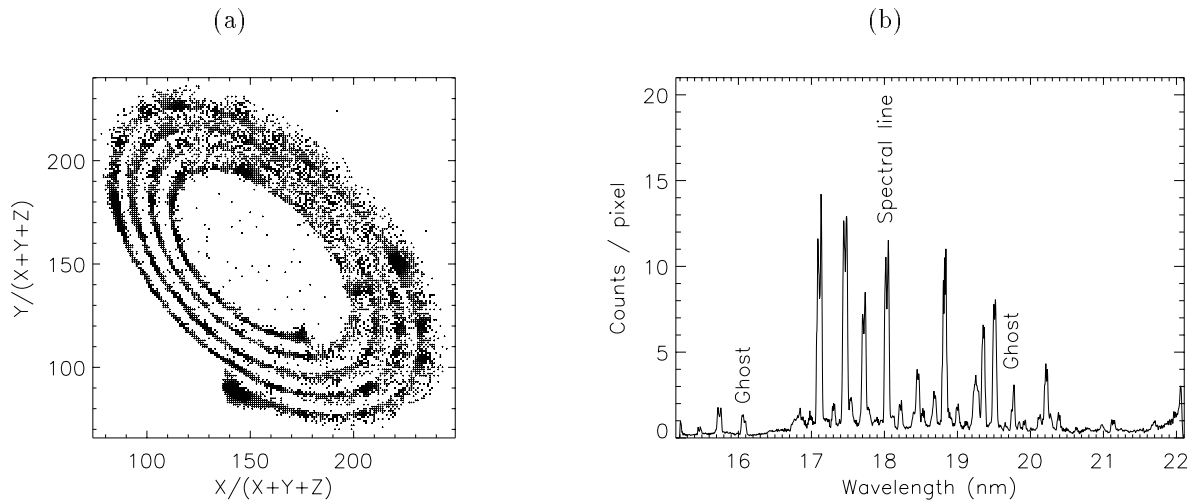


**Figure 8.** a) Plot of the normalized pulse heights in anodes  $X$  and  $Y$  from one of the CDS/GIS SPAN detectors, demonstrating the spectrum traces out a spiral. Note that at certain locations the spirals overlap, causing “ghosts”. b) A CDS/GIS spectrum. The spectral line at 18.05 nm also appears as “ghost” lines at 16.07 and 19.76 nm.

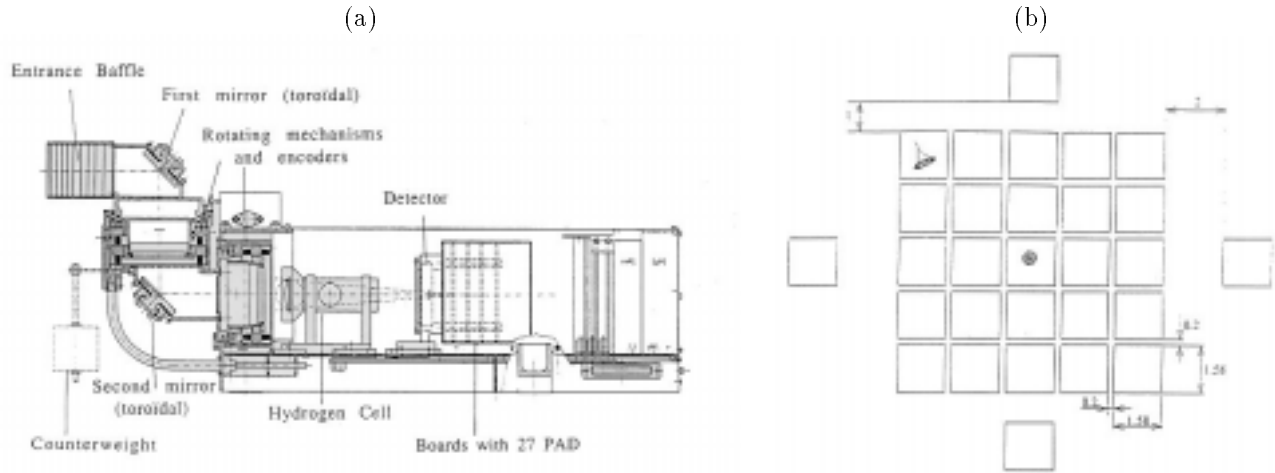


**Figure 9.** a) Diagram of the SWAN optics and detector system, showing the movable optics, hydrogen cell, and detector. b) The SWAN anode configuration. Sizes are in mm. Side pixels are used for dark current counting. In some pixels are shown the illumination pattern as computed from ray tracing.

This possible degradation is still being investigated. In late February 1999, one of the GIS detectors started to emit charged particles when under high voltage, causing increased background in all four detectors. When the high voltage for this particular detector was disabled, the increased background went away. Options for corrective action are under review. It is possible that this problem was induced by the extreme temperatures encountered during the months when SOHO was not under attitude control.

### 3.2. SWAN: A multi-anode MCP detector

The Solar Wind Anisotropies<sup>8</sup> (SWAN) experiment is designed to study the large-scale solar wind distribution, using scattered Lyman  $\alpha$  (121.6 nm) from interplanetary hydrogen atoms. There are two sensor units, mounted on opposite sides of the spacecraft, each of which can be pointed anywhere within  $2\pi$  steradians. In combination, the two sensor units are thus able to cover the entire celestial sphere except for avoidance zones around the Sun and Earth. Each sensor unit uses two concave toroidal mirrors to focus the radiation onto a  $\text{MgF}_2$  lens, which serves as the entrance window of a H cell (Figure 9a). Another  $\text{MgF}_2$  lens is used for the exit window of the H cell. By alternatively turning tungsten filaments on and off, the hydrogen switches between atomic and molecular, thereby either absorbing part of the Lyman  $\alpha$  line profile or allowing the full line profile to pass through to the detector. The operation of the H cell thus gives information about the Doppler shift and width of the line.

The SWAN detector system is a multi-anode MCP detector tube from Hamamatsu. The front window is a thick  $\text{MgF}_2$  flat window of 25 mm diameter, with a semi-transparent CsI cathode deposited on the inside. The signal is amplified by a microchannel-plate multiplier containing two stacks, and the charge is collected on a set of several square anodes (Figure 9b). Each anode is  $1.78 \times 1.78 \text{ mm}^2$ , corresponding to a square degree on the sky, and is connected to a Pulse Amplifier Discriminator (PAD), which selects pulses above a given threshold ( $\sim 10^5$  electrons) and sends them to a counter.

During the first three months of continuous observations, the sensitivity of the the  $+Z$  sensor increased by roughly 10%. After June 1996, and up until the loss of contact with SOHO in June 1998, only small changes were seen in the SWAN detectors. The  $-Z$  detector, which started out less sensitive than the  $+Z$  detector by a ratio of 1:2.6, showed no significant variation of sensitivity. Prior to the accident in June 1998, the sensitivity ratio at usual HV settings was equal to 1:2.9. It is believed that, with the standard HV setting for the MCP, only a fraction of the pulses are above the discriminator threshold, and that this fraction is smaller for the  $-Z$  detector than for the  $+Z$  detector, yielding the difference in sensitivity.

The loss-of-contact with the SOHO spacecraft did induce changes in the SWAN detectors. The sequence of events leading up to the shutting down of the spacecraft ended up leaving the sensors open to space. This caused the  $+Z$



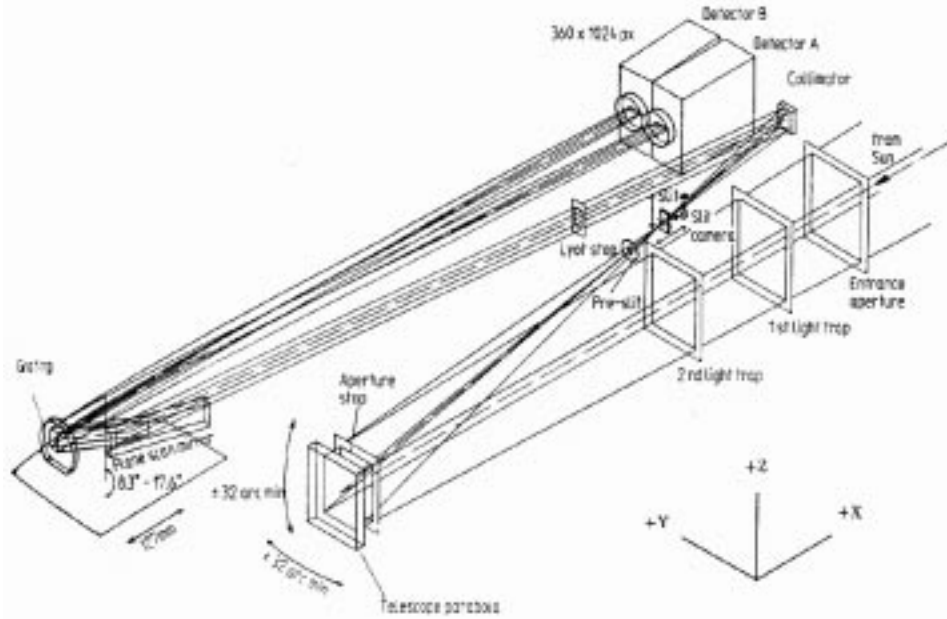


**Figure 10.** Schematic of the SUMER optics.

sensor to be on the hot side of SOHO, at a temperature larger than  $50^{\circ}\text{C}$  for two months, and possibly the  $+Z$  detector to be exposed to direct sunlight for an unknown amount of time. In consequence, the sensitivity in the center part of the  $+Z$  detector dropped by about 45%. In addition, the center pixels became partially sensitive to visible light, causing a larger sensitivity to cooler stars than before the accident. However, with the post-recovery recalibration and flat-field adjustments, measurements outside intensive star areas can be interpreted as before. The sensitivity could be increased by raising the detector voltage, but as this would lead to a higher probability of external event triggered over-current trips of the power supply, the voltage settings were not changed. The  $-Z$  detector was not exposed to direct sunlight and remained cold, and no changes were seen in that detector during the gap in operations.

### 3.3. Cross delay line detectors

Two of the instruments aboard SOHO, SUMER and UVCS, both use cross delay line<sup>9</sup> (XDL) detectors. Two of these detectors are used on SUMER, and two are used on UVCS. Each detector consists of a Z-stack of microchannel-plates. Readout is accomplished through a multilayer, cross delay-line anode. The basic design of each of the four detectors is identical, with only small differences. The SUMER detectors include electrostatic thermal ion deflectors, and meshes for Lyman  $\alpha$  attenuation as explained below. There is a  $\text{MgF}_2$  window on the UVCS Lyman  $\alpha$  detector, and a thermal ion rejection mesh covering the entrance aperture for the UVCS O VI detector. There are also differences in the photocathode coatings between the SUMER and UVCS detectors, as discussed below.

The solar conditions that the detectors were exposed to in the two instruments, and the experience that each instrument had with the detectors, is on the other hand quite different.

#### 3.3.1. SUMER: A cross delay-line detector on the solar disk

The Solar Ultraviolet Measurements of Emitted Radiation<sup>10</sup> (SUMER) experiment is a high resolution spectrograph operating from 66–161 nm in first order, and from 46–81 nm in second order. The telescope section consists of a single off-axis parabolic mirror, which can be swiveled to provide pointing and scanning capabilities. The solar image from the telescope is focused onto a narrow slit, which serves as an aperture to the spectrograph section (Figure 10). Within the spectrograph section, another off-axis parabola is used to recollimate the light. A plane scan mirror redirects this light onto a spherical grating, which then focuses the spectrally dispersed slit image onto the detector. By rotating the scan mirror, the angle of incidence on the grating is changed, thus changing the wavelengths which are focused onto the detector. The grating and scan mirror are mounted on a common platform which can be moved to maintain focus.

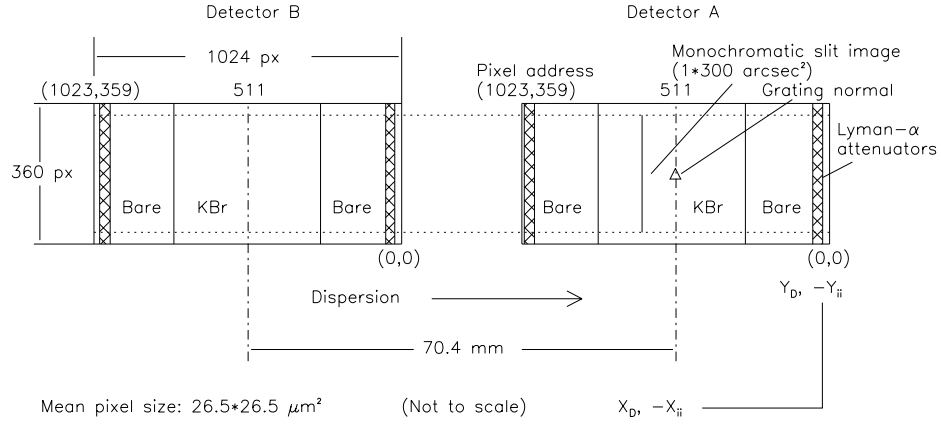


**Figure 11.** Schematic of the SUMER focal plane, showing the on-axis primary (A) detector, and the redundant (B) detector. Each detector has a KBr photocathode coated over the middle half, leaving the rest of the detector bare. The difference between the bare and KBr sensitivities can be used to distinguish first and second order lines. Attenuators cover the edges of both detectors for use with the bright Lyman  $\alpha$  line.

Two identical XDL detectors are mounted side-by-side at the focal plane. Only one detector is used at a time—the other detector provides redundancy. The central half of each detector’s field-of-view is coated with a KBr photocathode—the remainder of the detector is bare (Figure 11). Since the coated and uncoated sections of the detector will have different response curves as a function of wavelength, first and second order lines can be distinguished by placing them alternately on the coated and bare parts of the detectors. The extreme left and right edges of the detector are covered with meshes with nominal 10% transmission, 9 mm in front of the active surface of the detector. These grids can act as attenuators for the extremely strong Lyman  $\alpha$  line. Electrostatic thermal ion deflectors are also placed in front of the detector aperture to prevent ions from striking the MCP. The spectrometer itself is screened from charged particles entering any of the openings.

It is a regular part of the SUMER operational plan to vary the positions of bright lines, to even out the exposure on the detector. Even so, the solar UV flux ages the detector. In order to maintain the calibrated sensitivity of the detectors, the voltage on the MCP has been periodically incremented. With these voltage changes, the detector sensitivity has remained constant.<sup>11</sup> The original operating voltage across the MCP stack was 4835 V for the A detector, and 4620 V for the B detector. Each is now at 5500 V. The limit for each detector is 5700 V, so both detectors are now reaching the end of their calibrated lifetimes. To preserve the detectors into the solar maximum, SUMER has reduced operations to only observe about 25% of the time.

The detector edges—along the top and bottom, and those parts covered by the attenuation meshes (Figure 11)—only get limited exposure to light, and thus still have close to the original gain. With the voltage on the detector increased to overcome gain loss in the used portions of the detectors, any events that occur at the detector edges will cause a large cascade down the MCP pores, leading to noise spikes which leak inward to the used parts of the detector.

The XDL detectors, like most photon counting detectors, are subject to geometric distortions. The SUMER team has gone to great lengths to calibrate out the pincushion distortion of the detectors, but the time- and intensity-dependent nature of this distortion limits the accuracy with which Doppler shifts can be extracted from the data.

After SOHO’s accident, a small decrease in sensitivity was seen in data from both detectors. It is believed that this change is due to contamination of the optics, and that the detectors themselves remain unchanged.

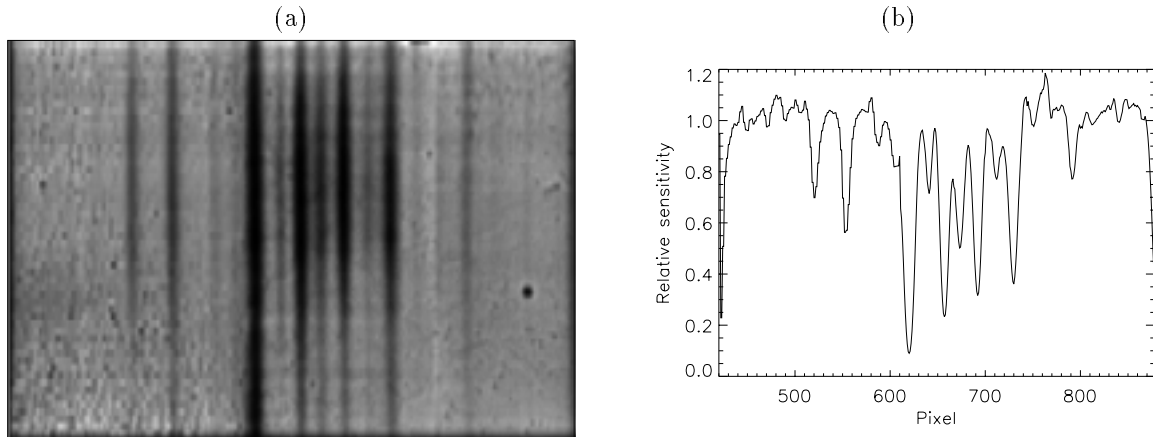


**Figure 12.** a) A portion of the UVCS flat field, showing the strong burn-in of the Lyman  $\alpha$  line on the detector. At various times the line was placed on different parts of the detector, so it appears burned-in at a number of locations. b) The average detector response for the detector pixels shown in (a).

### 3.3.2. UVCS: A cross delay-line detector in the solar corona

The Ultraviolet Coronal Spectrometer<sup>12</sup> (UVCS) is an occulted telescope and spectrometer experiment designed for observations in the extended solar corona. The instrument consists of two ultraviolet channels—one optimized for H I Lyman  $\alpha$  (121.6 nm), and the other for the O VI lines near 103.5 nm—as well as a white light polarimeter channel. The O VI channel includes a redundant optical path for H I Lyman  $\alpha$ . Both UV spectrographs are Rowland circle designs with toroidal gratings. Each grating is mounted in a Johnsons-Onaka configuration, and can rotate to scan a suitable spectral range through the detector field-of-view. This also allows the spectral lines to be moved on the detector so that bright lines do not always fall on the same pixels.

The XDL detectors used for each of the two ultraviolet channels are basically identical to those used for SUMER, except for the photocathode coating on the front face of the MCP stack. For UVCS, a KBr photocathode is coated over the full field-of-view of each detector. The detector used for the Lyman  $\alpha$  channel has a  $\text{MgF}_2$  window.

In the case of the O VI detector, the MCP current has been relatively constant. The voltage has been incrementally increased three times during the first three years of the mission to keep the pulse height distribution high as the detector ages. Nine more possible voltage increments remain. The O VI channel detector is operated in saturation mode, and the pulse height distribution is well situated between the upper and lower limit discriminators. The sensitivity is unchanged for this detector.

The experience with the Lyman  $\alpha$  detector is quite different. Over the course of the mission so far, changes were seen in the high voltage current of the Lyman  $\alpha$  detector. Part of this change could be attributed to seasonal temperature changes within the instrument, but there was also a steady increase in the current which could not be attributed to temperature. One possible explanation is that ion migration causes a chemical change in the #269 glass which changes the resistance. In September 1997, the high voltage was reduced to keep the current below 80  $\mu\text{A}$ . Figure 12 shows the flat field after the voltage change, for the 461 columns of the detector with the most use. There are an additional 514 columns with much less accumulated use. This detector is used primarily for H I Lyman  $\alpha$ , and so only about 50 columns are used for its observation at any one time. Weak spectral lines of S X, N V, and Fe XII are also occasionally observed. Since September 1997, the the regions of the detector with the highest use, seen as dark regions in Figure 12, have been avoided. Regions with the least use (a relative response of about 1.0) still have nearly saturated pulse height distributions, and so their efficiencies are nearly the same as for the beginning of the mission. The regions with a 10% drop in relative response or greater produce an approximately corresponding fraction of their pulses below the threshold. This fraction is dependent on the absolute dose. The UVCS team has found that  $1.5 \times 10^5$  total counts/pixel corresponds to an apparent 10% drop in relative response with the post-September 1997 detector voltage setting. The flat field characterization is kept updated during the

Instrument	Maximum counts/pix/s	
	Theoretical	“Typical”
CELIAS/SEM	100,000	80,000
EIT	6800	2700
CDS/NIS	87,000	600
CDS/GIS	1000	60
SWAN	-	-
SUMER	400	40
UVCS	400	10

**Table 1.** Comparison of the maximum count rate capability of each instrument. Also shown are “typical” extreme count rates encountered in flight. A line separates the analog from the photon counting detectors. See text for notes pertaining to the individual instruments.

flight so it can be used with good precision to correct regions of the detector with relative responses above 50%. The corrections can be checked by making simultaneous measurements with the redundant path of the O VI channel.

The regions of the detector with reductions in gain were found to have an effective decrease in resolution. This effect was quantified by making simultaneous measurements with the redundant path of the O VI channel. The regions of highest use can have effective resolution elements as large as three pixels compared to one pixel for a saturated distribution. The origin of this effect is still under investigation, but seems to be associated with a timing uncertainty resulting from the small charge of the XDL pulses.

The Lyman  $\alpha$  detector also has regions with increased detector background. Some of this appears to be caused by an increased number of thermal electrons emitted by the higher temperature channel plate. An intermittent component that has effected a small portion of the detector may be due to field emission.

No changes were seen in either UVCS detector as a result of SOHO’s accident in the summer of 1998.

#### 4. CONCLUSIONS

The UV detectors aboard SOHO have worked well over the first three years of the mission, and are still taking scientific data. All the detectors survived the catastrophic loss and subsequent recovery of SOHO during the summer and fall of 1998 with little or no damage.

A number of the UV detectors show burn-in effects from long-term exposure. Such burning in is to be expected for MCP-based detectors, but the burning in of backside-thin CCD used on EIT was a surprise. It is not yet clear whether this is endemic to this technology, or specific to the EIT detector. A worthwhile goal for future solar UV detector work is to increase detector longevity.

Count rate capability is an important factor for solar UV detectors. Table 1 compares the maximum count rates for the different instruments. The following are some comments on the individual instruments:

- The EIT count rate capability is primarily limited by the shutter—EIT also has a shutterless mode, where the maximum count rate can go up to 136,000 counts/pix/s.
- The maximum count rate for the CDS/NIS detector depends on the voltage applied to the MCP. At 600 V, the maximum count rate would be closer to 820,000. The limit of the linear response regime is lower than this, at about 2200 for the current operating voltage, or 21,000 at 600 V.
- The number quoted for the theoretical SUMER pixel limitation is appropriate for a point source. However, tests both in the lab and in flight with a slit aperture show that a local gain depression starts becoming a problem for a line source at around 10–30 counts/pix/s.<sup>13</sup> A calibration procedure has been implemented to correct for the short-term gain depression at the higher count rates, but the SUMER team recommends staying below 10 counts/pix/s for the most accurate calibration. Higher count rates have, however, been seen regularly throughout the mission.

- The UVCS team tries not to go above 3 counts/pix/s, to preserve the detector lifetime.

Although photon counting detectors have proven useful on SOHO, Table 1 clearly demonstrates the importance of analog UV detectors for many aspects of solar physics.

## ACKNOWLEDGMENTS

A paper such as this would not be possible without a great deal of support from each of the instrument teams. I would like to thank each of the SOHO instrument teams mentioned in the above report, for their support in providing information about their instruments, for providing figures, for reviewing this report for accuracy, and even on occasion for supplying suggested text about their instruments. In particular, I would like to thank the following team members: SEM: Howard Ogawa; EIT: Dan Moses, Jeff Newmark; CDS: Richard Harrison, Eddie Breeveld; SWAN: Jean-Loup Bertaux, Walter Schmidt, Eric Quemerais; SUMER: Klaus Wilhelm, Udo Schühle, Werner Curdt, Terry Kucera; UVCS: John Kohl, Joe Michels, Nigel Atkins, Larry Gardner.

## REFERENCES

1. D. Hovestadt *et al.*, “CELIAS—Charge, Element and Isotope Analysis System for SOHO,” *Solar Phys.* **162**, pp. 441–481, 1995.
2. D. L. Judge, D. R. McMullin, H. S. Ogawa, D. Hovestadt, B. Klecker, M. Hilchenbach, E. Möbius, L. R. Canfield, R. E. Vest, R. Watts, C. Tarrío, M. Kühne, and P. Wurz, “First solar EUV irradiances obtained from SOHO by the CELIAS/SEM,” *Solar Phys.* **177**, pp. 161–173, 1998.
3. H. S. Ogawa, D. L. Judge, D. R. McMullin, P. Gangopadhyay, and A. B. Galvin, “First-year continuous solar EUV irradiance from SOHO by the CELIAS/SEM during 1996 solar minimum,” *J. of Geophys. Res.* **103**, pp. 1–6, 1998.
4. J.-P. Delaboudinière *et al.*, “EIT: Extreme-ultraviolet Imaging Telescope for the SOHO Mission,” *Solar Phys.* **162**, pp. 291–312, 1995.
5. D. Moses *et al.*, “EIT observations of the extreme ultraviolet Sun,” *Solar Phys.* **175**, pp. 571–599, 1997.
6. R. A. Harrison *et al.*, “The Coronal Diagnostic Spectrometer for the Solar and Heliospheric Observatory,” *Solar Phys.* **162**, pp. 233–290, 1995.
7. W. T. Thompson, A. I. Poland, O. H. W. Siegmund, M. Swartz, D. B. Leviton, and L. J. Payne, “Measurements of an intensified CCD detector for the Solar and Heliospheric Observatory,” in *EUV, X-ray and Gamma-Ray Instrumentation for Astronomy III, Proc. SPIE* **1743**, pp. 464–474, 1992.
8. J. L. Bertaux *et al.*, “SWAN: A study of solar wind anisotropies on SOHO with Lyman alpha sky mapping,” *Solar Phys.* **162**, pp. 403–439, 1995.
9. O. H. W. Siegmund, J. M. Stock, D. R. Marsh, M. A. Gummin, R. Raffanti, J. Hull, G. A. Gaines, B. Welsh, B. Donakowski, P. Jelinsky, T. Sasseen, and J. L. Tom, “Delay line detectors for the UVCS and SUMER instruments on the SOHO satellite,” in *EUV, X-ray and Gamma-Ray Instrumentation for Astronomy V, Proc. SPIE* **2280**, pp. 89–100, 1994.
10. K. Wilhelm *et al.*, “SUMER—Solar Ultraviolet Measurements of Emitted Radiation,” *Solar Phys.* **162**, pp. 189–231, 1995.
11. U. Schühle, P. Brekke, W. Curdt, J. Hollandt, P. Lemaire, and K. Wilhelm, “Radiometric calibration tracking of the vacuum-ultraviolet spectrometer SUMER during the first year of the SOHO mission,” *Applied Optics* **37**, pp. 2646–2652, 1998.
12. J. L. Kohl *et al.*, “The Ultraviolet Coronal Spectrometer for the Solar and Heliospheric Observatory,” *Solar Phys.* **162**, pp. 313–356, 1995.
13. K. Wilhelm *et al.*, “First results of the SUMER telescope and spectrometer on SOHO,” *Solar Phys.* **170**, pp. 75–104, 1997.